

# Multichannel Quantum Defect Theory (MQDT) Analysis of the (2 + 1') Mass Analyzed Threshold Ionization (MATI) Spectroscopy of NH<sub>3</sub><sup>†</sup>

H. Dickinson, D. Rolland,<sup>‡</sup> and T. P. Softley\*

Physical and Theoretical Chemistry Laboratory, South Parks Road, Oxford, OX1 3QZ, United Kingdom

Received: October 12, 2000; In Final Form: January 9, 2001

MATI spectra of NH<sub>3</sub> have been recorded using two-color (2 + 1') multiphoton excitation via the  $\tilde{B}$  and  $\tilde{C}'$  states and have been simulated using multichannel quantum defect theory. New vibrational bands in the MATI spectra are reported for intermediate levels up to  $\nu_2 = 6$  in the  $\tilde{B}$  state. The spectra obtained should in principle be identical to ZEKE spectra recorded under the same resolution. A good agreement between experiment and theory is obtained by using quantum defects determined previously from optical spectra and optimization of unknown parameters. The effects of  $p\pi-d\delta$  mixing in the core region are included to account for "forbidden" transitions, and the optimization of quantum defect parameters is used to quantify the strength of this mixing. Molecular symmetry group arguments are used to define which channels must be included in the quantum defect matrix. The paper demonstrates that in favorable cases a complete theory of ZEKE/MATI line intensities is achievable including the effects of bound-state couplings.

## 1. Introduction

In a previous paper,<sup>1</sup> hereinafter referred to as Paper I, we reported the observation of the rotationally resolved (2 + 1') MATI spectra of ammonia using the  $\tilde{C}'$  state as the intermediate at the two-photon level. We also discussed a preliminary attempt to model the rotational line intensities using MQDT. The present paper reports an extension of that methodology to include  $l$ -mixing in the core region and the application of the theory to a wide range of MATI spectra obtained via both the  $\tilde{B}$  and  $\tilde{C}'$  states of ammonia. An excellent level of agreement between experimental and theoretical line intensities is achieved using only a small number of input parameters for the calculations. New experimental spectra recorded via levels up to  $\nu_2 = 6$  of the  $\tilde{B}$  state intermediate are also reported.

The advent of ZEKE spectroscopy in the laboratory of Schlag and Müller-Dethlefs<sup>2,3</sup> and of the analogous technique MATI spectroscopy<sup>4</sup> in the 1990s has allowed, among many other benefits, a new detailed view of the dynamics of photoionization near threshold. Although in most cases the fitting of rotationally resolved spectral line positions has been relatively straightforward (CH<sub>4</sub><sup>+</sup> being a notable exception<sup>5</sup>), the interpretation of intensities, in almost every case where rotational structure has been observed, is complicated by channel interactions among the Rydberg series and continua.

To date a variety of approaches to the problem of ZEKE/MATI transition intensities in polyatomics have been proposed. McKoy and co-workers have taken an ab initio approach to calculation of the ZEKE or threshold photoelectron spectra of small polyatomic hydrides.<sup>6–9</sup> Generally applicable propensity rules for the photoionization process in symmetric and asymmetric tops can be extracted from their model. These make no assumptions about the nature of the orbital from which the photoelectron is ejected and an ab initio calculation is carried out to determine the orbital character. Although a good match

to experimental results has been obtained in many cases, small (but significant) deviations remain because these calculations do not include the interactions between bound Rydberg states and the photoionization continuum. Continuum-continuum couplings are included however and these are closely related to the bound state interactions. A related model, using symmetry arguments to predict allowed transitions and intensities, has been proposed by Müller-Dethlefs<sup>10</sup> and applied by him to the ZEKE spectrum of ammonia via the  $\tilde{B}$  state.<sup>11</sup> The model incorporates some aspects of the MQDT frame transformations presented in our work, but does not include the effects of bound-state channel interactions and hence does not fully explain the experimental data. Signorell and Merkt have proposed a set of general symmetry selection rules for photoionization of polyatomics<sup>12</sup> using the molecular symmetry group. These rules are based solely on group theoretical considerations and assume conservation of the total angular momentum only, hence providing a listing of all ionic states accessible from a particular intermediate state. These rules provide a very useful general framework but they make no distinction between direct transition intensity to the channel of interest and indirect access via channel couplings; thus, they are all-embracing but do not necessarily provide insight into the intensity mechanisms at work in a ZEKE or MATI spectrum.

In our work, which has developed from the first application of MQDT to the ZEKE spectrum of H<sub>2</sub>,<sup>13</sup> the symmetry arguments of Signorell and Merkt are used to determine which channels need to be considered explicitly in the excitation from an initial level, and these are then combined with a MQDT treatment to find relative intensities. The MQDT approach incorporates all channel interactions but requires only the quantum defects and dipole transition moments as input parameters. The advantage of this approach is that it is able to include bound states and continua within a single formalism. Our aim is to develop a "complete" theory of ZEKE/MATI line intensities.

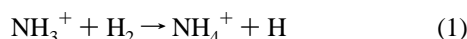
An additional motivation for our work is to investigate the creation of state-selected NH<sub>3</sub><sup>+</sup> ions. This would open up the

<sup>†</sup> Part of the special issue "Edward M. Schlag Festschrift".

\* To whom correspondence should be addressed.

<sup>‡</sup> Present address; IAMS Academia Sinica, 1 Roosevelt Rd Sec 4, Taipei 106, ROC Taiwan.

possibility of studying the effect of variation in the projection quantum number  $K$  on the reaction cross section for ion–molecule reactions. In effect, this could amount to comparing the effect of spinning-top axial rotation with end-over-end rotation about an axis perpendicular to the symmetry axis. In astrophysically important processes such as



which take place in interstellar nebulae at temperatures as low as 10 K, rotational effects on the reaction cross section might be significant.

The two states used as intermediates in the  $(2 + 1)$  MATI spectra reported in this paper are the  $\tilde{B} \ ^1E''$  and  $\tilde{C}' \ ^1A_1'$  states, accessed by the perpendicular  $1a_2'' \rightarrow 3pe'$  and parallel  $1a_2'' \rightarrow 3pa_2''$  electronic promotions, respectively. Photoionization out of different vibrational levels of these states displays largely diagonal Franck–Condon factors due to the similar bond lengths and geometries in the Rydberg state and ion. A  $\Delta v_2 = v_2^+ - v_2 = 0$  contribution of  $>80\%$  through the  $\tilde{C}'$  state and  $>70\%$  through the  $\tilde{B}$  state is observed in photoionization,<sup>14</sup> and has been used as a source of vibrationally state-selected  $\text{NH}_3^+$  ions for reaction dynamics studies.<sup>15</sup> These observations suggest we should anticipate intense MATI transitions to states with the same vibrational quantum numbers in the Rydberg state and ion. There is a significant difference between the  $\tilde{B}$  and  $\tilde{C}'$  states in that the  $3pe'$  Rydberg orbital in the  $\tilde{B}$  state has a significant degree ( $>10\%$ ) of  $3de'$  character mixed in whereas the  $\tilde{C}'$  state is almost pure  $p$  character as there is no  $3d$  state of  $a_2''$  symmetry.

## 2. Experimental Procedures and Results

The experimental apparatus has been described in Paper I. In brief a supersonic skimmed molecular beam of  $\text{NH}_3$ , diluted to 10% in argon, is crossed perpendicularly by two laser beams provided by a dye laser (Quanta Ray PDL 3) and an optical parametric oscillator (Quanta Ray MOPO 730) both pumped at 355 nm by a frequency-tripled injection-seeded Nd:YAG laser (GCR 290) operating at 10 Hz, 10 ns pulse length. The REMPI signal is obtained by accelerating the ions in the molecular beam direction to an MCP detector. The MATI pulsed-field ionization spectra are obtained by discriminating against prompt ions using a retarding potential applied parallel to the beam direction and then ionizing the high- $n$  Rydberg states using a delayed pulsed field. Figure 1 shows the typical one-laser REMPI and two-laser REMPI + MATI time-of-flight signals.

**2.1.  $(2 + 1)$  REMPI Spectrum of Ammonia.** The  $(2 + 1)$  resonance enhanced multiphoton ionization spectrum of ammonia in the region  $60000\text{--}67250\text{ cm}^{-1}$  (one-photon wavelength range  $333\text{--}297\text{ nm}$ ) is shown in Figure 2. The spectrum shows transitions to both the  $\tilde{C}'$  and  $\tilde{B}$  states, with long progressions in the  $v_2$  “umbrella” bending mode, as discussed above. The simple appearance of the spectrum is due to the significant rotational cooling ( $T < 15\text{ K}$ ) in the supersonic expansion of the molecular beam, which results in only the  $0_0$ ,  $1_1$ , and  $1_0$  levels of the ground state being significantly occupied (the notation used is  $J_K$ ). Transitions were assigned by comparison with the work of Conaway et al.<sup>14</sup> and confirmed in this work by spectral simulation using the  $\tilde{C}'$  state constants from Nieman and Colson<sup>16</sup> and Ashfold et al.,<sup>17</sup> and the  $\tilde{B}$  state constants determined from a high resolution study also by the Ashfold group.<sup>18</sup> A typical pair of vibrational bands and the simulation of them is shown in Figure 3.

**2.2. The  $(2 + 1)$  MATI Spectra of Ammonia.** 2.2.1. *General Features of the MATI Spectra.* The MATI spectra were

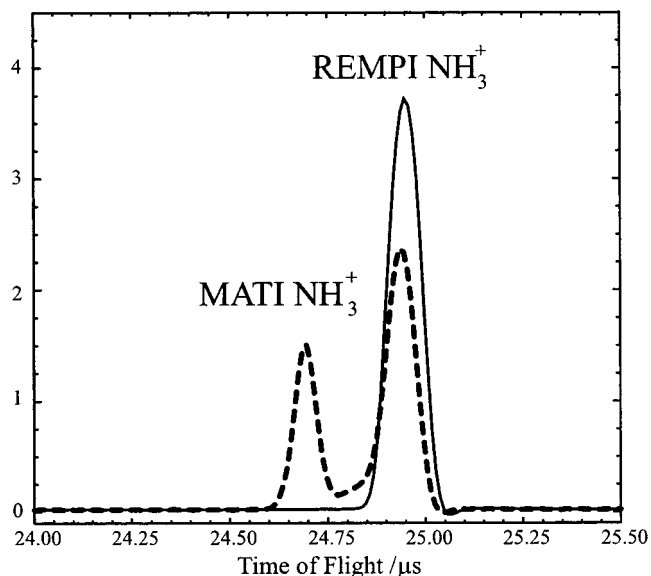


**Figure 1.** Time-of-flight profile showing the REMPI and MATI peaks for ammonia. Bold line, laser 1 only present; dashed line, with laser 2 tuned to the MATI resonance.

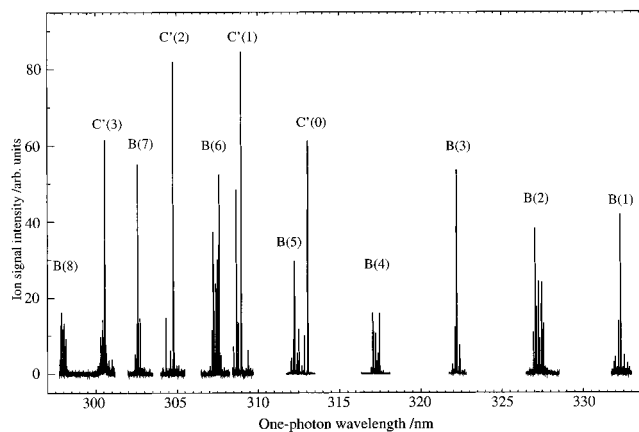


**Figure 2.**  $(2+1)$  REMPI spectrum of ammonia. The spectrum has not been corrected for any variation in laser power due to the laser dye curve.

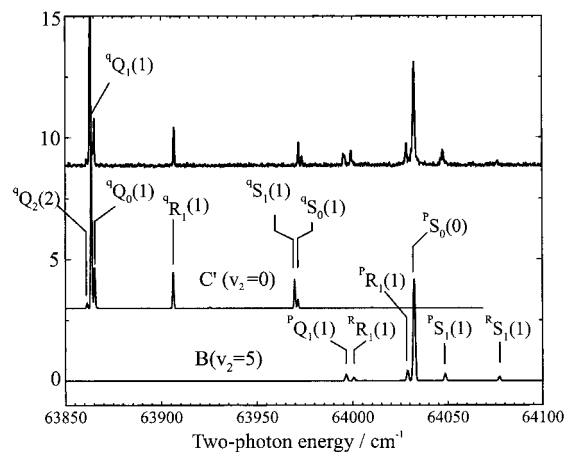


**Figure 3.**  $2+1$  REMPI spectrum via the  $\tilde{B} (v_2 = 5)$  and  $\tilde{C}' (v_2 = 0)$  states with (a) experiment and (b,c) rotational line strength simulation.

recorded by applying a continuous discrimination field of  $0.46\text{ V/cm}$  in the direction parallel to the molecular beam followed by a delayed pulsed field of  $5\text{ V/cm}$  to ionize the Rydberg states. It was found that the use of a significantly larger discrimination field led to the elimination of the MATI signal, presumably

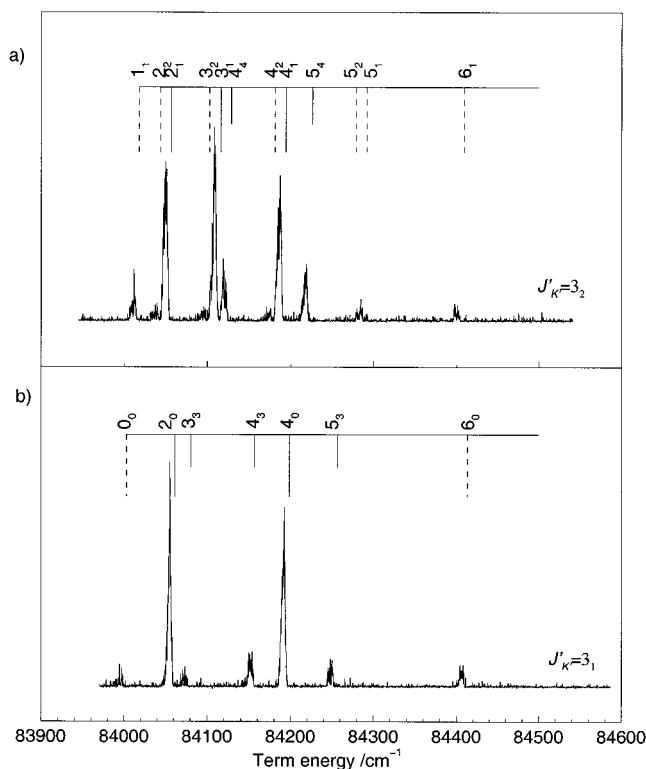


**Figure 4.** MATI spectra of  $\text{NH}_3$  with excitation from different rotational levels of the  $\tilde{B}(2)$  state; (a) via the para  $3_2$  level and (b) via the ortho  $3_1$  level. Ionic thresholds  $N_{K^+}$  are indicated above the spectrum; long solid lines indicate thresholds accessible from a  $p\pi$  intermediate, short solid lines indicate thresholds accessible from a  $d\delta$  intermediate and dashed lines indicate thresholds inaccessible according to the rotation spectator model (see text).

due to Rydberg state lifetime effects.<sup>19</sup> Some typical spectra via the  $\tilde{B}$  state are shown in Figures 4–6. The spectra recorded via various intermediate rotational states of the  $\tilde{C}$  state were shown previously in Paper I and some of these are reproduced in Figures 7–11. Related ZEKE spectra via the  $3_2$  and  $3_1$  levels of the  $\tilde{B}$   $v_2 = 2$  state were first reported by Habenicht et al.,<sup>11</sup> while nonresonant two-photon ZEKE and one-photon VUV ZEKE spectra have also been recorded previously.<sup>20,21</sup>

Each spectrum consists of a number of well-separated and readily identifiable peaks, demonstrating that state-selection of the  $N^+$  and  $K^+$  quantum numbers for a wide variety of  $v_2$  vibrational levels is possible using this method. The peaks observed in the spectra were assigned by calculating their term energy  $F$  above the ground-state according to

$$F(v_2^+, N^+, K^+) = \text{IE} + G(v_2^+) + BN^+(N^+ + 1) + (C - B)K^{+2} \quad (2)$$

where IE is the adiabatic ionization energy of the molecule,  $G(v_2^+)$  the internal vibrational energy of the ion, and the other symbols have their usual significance. The ionization threshold of  $82159.1 \text{ cm}^{-1}$  is obtained from the work of Reiser et al.,<sup>21</sup> while an IR study by Lee and Oka<sup>22</sup> provided the ionic rotational constants. In the spectra presented in Figures 4–6, the field-free ionic thresholds for each peak are marked above the spectrum. As expected, the MATI peaks are slightly red-shifted with respect to the field-free thresholds.

**2.2.2. Zero-Order Selection Rules.** As described in paper I, we can determine the basic propensity rules based on a zero-order model with the intermediate state treated as Hund's case (b) and the final state as Hund's case (d). These rules may be

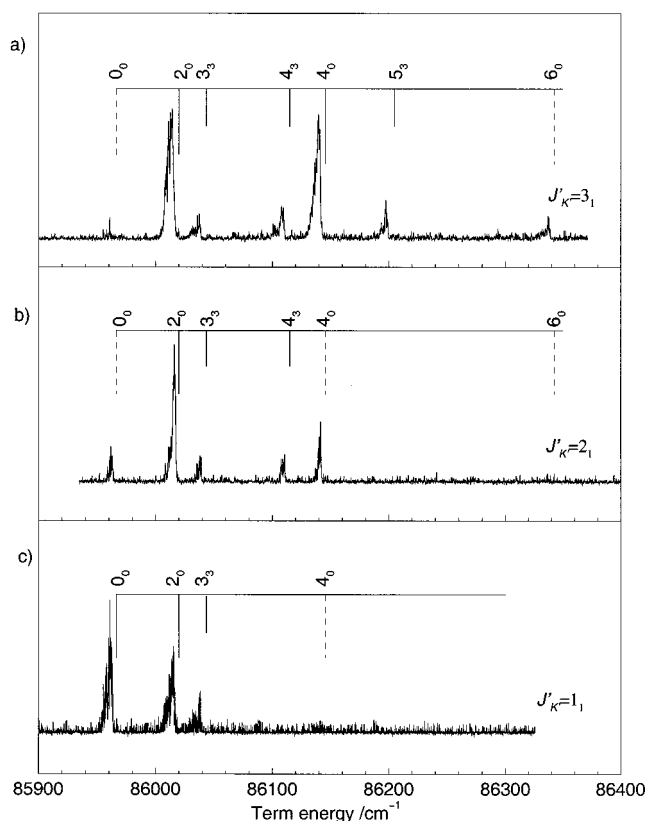


**Figure 5.** MATI spectra of  $\text{NH}_3$  with excitation from different ortho rotational levels of the  $\tilde{B}(4)$  state; (a) via the  $3_1$  level, (b) via the  $2_1$  level, and (c) via the  $1_1$  level. Ionic thresholds  $N_{K^+}$  are indicated above the spectrum; long solid lines indicate thresholds accessible from a  $p\pi$  intermediate, short solid lines indicate thresholds accessible from a  $d\delta$  intermediate and dashed lines indicate thresholds inaccessible according to the rotation spectator model (see text).

stated as follows:

$$N^+ = J' + I' \quad (3)$$

$$K^+ = K' - \lambda' \quad (4)$$

where  $K^+$ ,  $\lambda'$ , and  $K'$  are the projections along the  $C_3$  symmetry axis of the total angular momentum of the ion excluding spin ( $N^+$ ), the Rydberg electron orbital angular momentum in the intermediate state ( $I'$ ), and the total angular momentum in the intermediate state, ( $J'$ ) respectively. (Throughout the remainder of this paper, quantum numbers of the ground state, intermediate ( $\tilde{B}$  or  $\tilde{C}'$ ) state, final high- $n$  Rydberg states and ion are distinguished by double primes ( $''$ ), single primes ( $'$ ), no sub/superscripts, and plusses (+) respectively.) The projection quantum numbers in eq 4 can each take positive and negative values in the present formulation. The “descent of symmetry” correlation between the  $D_{3h}$  symmetry labels for the excited electron ( $e'$  for the  $\tilde{B}$  state and  $a_2''$  for the  $\tilde{C}'$  state) and the  $\lambda$  quantum number (strictly only a good quantum number in  $D_{\infty h}$ ) is shown in Table 1. The first selection rule above, eq 3, expresses the conservation of angular momentum within the rotation spectator model,<sup>24</sup> in which it is assumed that the photon angular momentum  $\gamma$  is consumed only by the electron so that  $\mathbf{l} = \mathbf{I}' + \boldsymbol{\gamma}$ . An additional requirement is that nuclear spin symmetry be conserved throughout the transition, i.e., *ortho*  $\leftrightarrow$  *ortho* and *para*  $\leftrightarrow$  *para* but *ortho*  $\nleftrightarrow$  *para*.

**2.2.3. Comparison of Zero-Order Selection Rules with the MATI Spectra via the  $\tilde{C}'$  State.** Use of eq 4 implies that in the

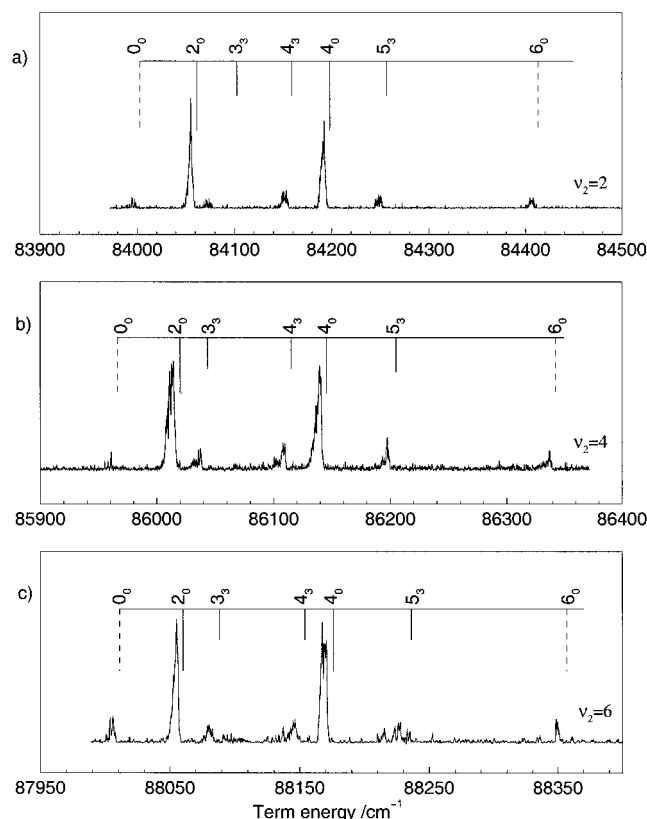


**Figure 6.** MATI spectra of  $\text{NH}_3$  recorded (a) via the  $\tilde{B}(2) 3_1$  level, (b) via the  $\tilde{B}(4) 3_1$  level, and (c) via the  $\tilde{B}(6) 3_1$  level.

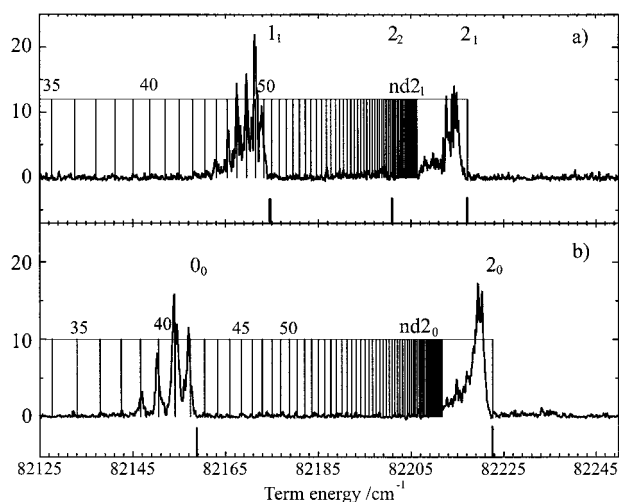


**Figure 7.** Channel interactions in the MATI spectrum with excitation (a) via the  $\tilde{C}'(0) 1_1$  level, (b) via the  $\tilde{C}'(0) 1_0$  level. The Rydberg series  $nd 2_1$  and  $nd 2_0$  are marked in (a) and (b), respectively.

MATI spectra recorded via the  $\tilde{C}' 3p a_2''$  Rydberg state, for which  $\lambda' = 0$ , peaks corresponding to  $\Delta K^+ = 0$  only should be observed (where  $\Delta K^+ = K^+ - K'$ ). The dominant transitions in each spectrum are indeed those predicted according to the model described above e.g., in Figure 9, the main transitions observed via the  $2_1$  level are to the  $1_1, 2_1,$  and  $3_1$  states. However, transitions breaking the constraints on  $N^+$  required by the rotation spectator model and transitions accompanied by anomalous changes in the  $K$  quantum number are both observed, and are listed in Table 2. In addition, several of the peaks show fine structure with 2–3 subpeaks evident within the main peak. For example, the  $0_0$  peak in the spectrum via the  $\tilde{C}'(0) 1_0$  state (shown in Figure 8) and the  $1_1$  peak in the spectrum via the

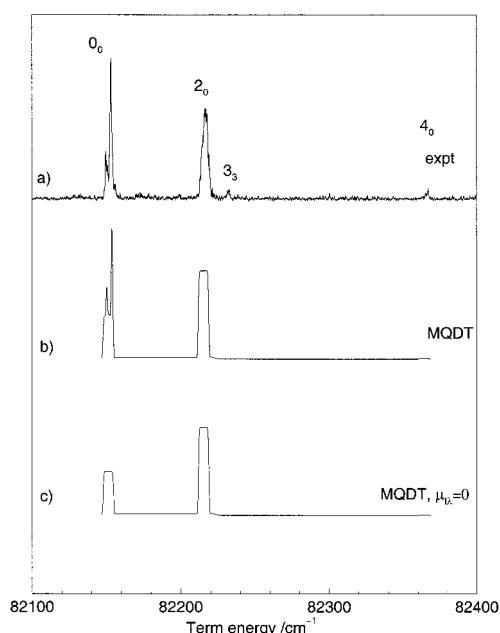


**Figure 8.** MATI spectrum via the  $\tilde{C}'(0) 1_0$  level; (a) experimental spectrum, (b) MQDT simulation, parameters as described in the text and (c) MQDT simulation, all quantum defects set to zero.

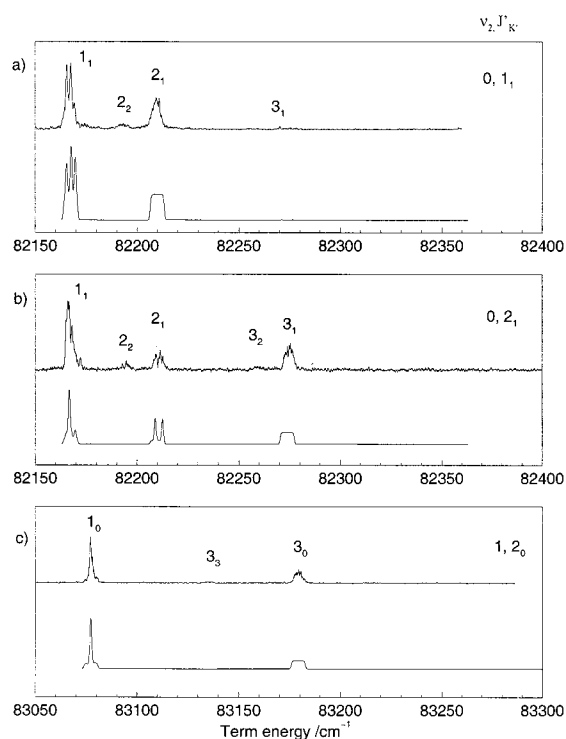


**Figure 9.** MATI spectra (upper trace) and MQDT simulations (lower trace) via (a) the  $\tilde{C}'(0) 1_1$  level, (b) the  $\tilde{C}'(0) 2_1$  level and (c) the  $\tilde{C}'(1) 2_0$  level.

$\tilde{C}'(0) 1_1$  state (Figure 9a), each show substructure. In Figure 7 these peaks have been recorded with a larger extraction field, broadening the field-ionization range to reveal more of the underlying Rydberg structure. These observations are a characteristic signature of channel interactions between Rydberg series converging on different ionic rotational states.

As discussed in many previous publications, e.g., ref 24, interaction between the Rydberg electron and the ion core can induce coupling between Rydberg series of the same total symmetry and angular momentum. If this coupling is between a bound Rydberg state and an isoenergetic pseudocontinuum

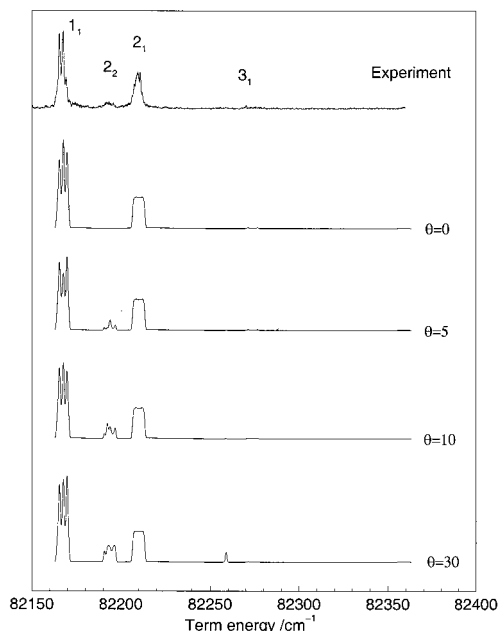


**Figure 10.** Effect of increasing the  $p\pi/d\delta$  mixing angle on the MQDT simulation for excitation via the  $\tilde{C}'(0) 1_1$  level.

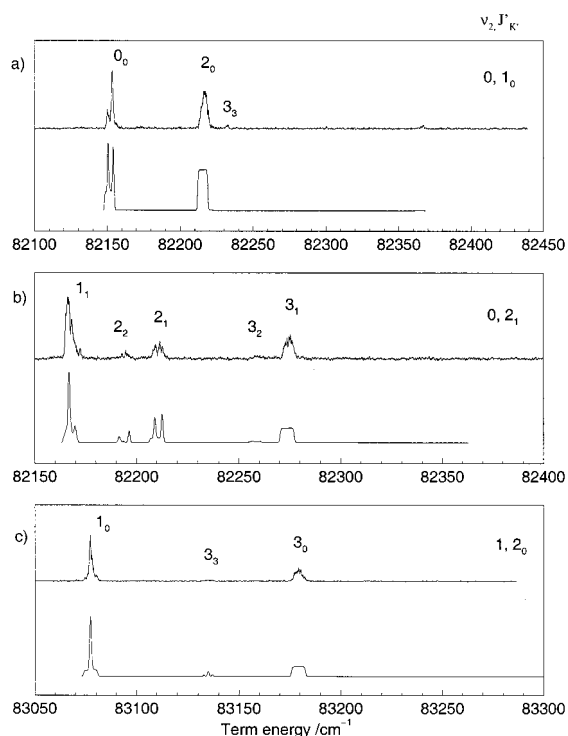


**Figure 11.** MATI spectra (upper trace) and MQDT simulations (lower trace), including a  $p\pi/d\delta$  mixing angle of  $5^\circ$ , via (a) the  $\tilde{C}'(0) 1_0$  level, (b) the  $\tilde{C}'(0) 2_1$  level and (c) via the  $\tilde{C}'(1) 2_0$  level.

**TABLE 1: Correlation of Electron Symmetries from  $D_{\infty h}$  to  $D_{3h}^a$**

$l\lambda$	$l$ even	$l$ odd
$ 0\rangle$	$a_1'$	$a_2''$
$ l \pm 1\rangle$	$e_1''$	$e_2'$
$ l \pm 2\rangle$	$e'$	$e''$
$ l \pm 3\rangle$	$a_2' + a_1'$	$a_1' + a_2'$

<sup>a</sup>From ref 23.

converging on a lower ionic threshold, the interaction can cause intensity enhancements in the MATI (or ZEKE) peak corresponding to the lower threshold, at the energies of the bound

**TABLE 2: Forbidden Peaks Observed in MATI Spectra via Various Intermediate Rotational Levels of the  $\tilde{C}'$  State**

intermediate level	"forbidden" peaks
$v_2, J_K'$	
0, $1_0$	$4_0 3_3$
0, $1_1$	$3_1 2_2$
0, $2_1$	$2_2 3_2$
1, $2_0$	$3_3$

Rydberg state, converging to the higher threshold. For example, the sub peaks in the  $1_1$  peak can be fitted to a Rydberg series converging on the  $2_1$  threshold, as illustrated in Figure 7a. As pointed out in Paper I, the same basic mechanism can also couple an optically accessible *continuum* and isoenergetic pseudocontinuum. Such an interaction is shown below to give rise to the observed intensity in the "forbidden"  $4_0$  peak of Figure 8. The effect of channel interactions is evident in several of the spectra, other examples including the  $3_3$  peak ( $\Delta K^+ = 3$ ) in the spectra via both the  $\tilde{C}'(1) 2_0$  state (Figure 9(c)) and the  $\tilde{C}'(0) 1_0$  state (Figure 8), or the  $K^+ = 2$  peaks ( $\Delta K^+ = 1$ ) in the spectra via the  $\tilde{C}'(0) 1_1$  and  $2_1$  states shown in Figure 9a,b.

The intensity perturbations caused by Rydberg electron/core interactions are a dominant feature of these spectra. The origin of these perturbations, and detailed modeling of the perturbed intensities, is the central theme of this paper and will be addressed in the following sections.

**2.2.4. MATI Spectra via the  $\tilde{B}$  State.** Figures 4 and 5 show MATI spectra recorded via various rotational levels of the  $\tilde{B}(2)$  and  $\tilde{B}(4)$  states. The  $\tilde{B}$  state has a total electronic symmetry of  $\tilde{E}''$ , which can be decoupled into a product of the ion-core electronic symmetry  $A_2''$  and Rydberg electron symmetry  $e'$ . By reference to Table 1, it can be seen that  $e'$  correlates with either a  $p\pi$  or  $d\delta$  electron in  $D_{\infty h}$ . In early work the  $\tilde{B}$  state was assumed to be purely  $p\pi$ , due to its large quantum defect of 0.81.<sup>25</sup> However, the  $(2+1')$  ZEKE spectra recorded via the  $\tilde{B}$  state by Habenicht et al. could only be interpreted by assuming some degree of  $d\delta$  character.<sup>11</sup> Application of eq 4 therefore leads to a selection rule of  $\Delta K^+ = \pm 1$  if excitation occurs from a  $p\pi$  orbital component or  $\Delta K^+ = \pm 2$  from a  $d\delta$  orbital component (subject to the additional constraints of nuclear spin symmetry conservation). In Figures 4 and 5, states accessible according to the  $\Delta K^+ = \pm 1$  selection rule are indicated by long vertical lines above the spectrum while those accessible according to  $\Delta K^+ = \pm 2$  are identified by shorter vertical lines.

The  $\Delta K^+ = \pm 1$  transitions dominate the less intense  $\Delta K^+ = \pm 2$  transitions, as expected. Nevertheless, there still remain some additional peaks unaccounted for. Transitions involving large, forbidden values of  $\Delta N^+$  are seen, such as the clear transition to the  $6_0$  level in the spectrum via the  $\tilde{B}(4) 3_1$  state (Figure 5a) or the transitions to  $1_1$ ,  $5_1$  and  $6_1$  levels observed via the  $\tilde{B}(2) 3_2$  state (Figure 4a). These transitions with anomalous changes in  $N^+$  can again, as in the spectra via the  $\tilde{C}'$  state, be attributed to interactions between channels of the same total symmetry. In addition to the transitions accompanied by anomalous changes of  $\Delta N^+$ , transitions involving forbidden changes in  $K$  quantum number occur. Examples are the  $K^+ = 2$  states, corresponding to a  $\Delta K^+ = 0$  transition, seen in the spectrum via the  $3_2$  rotational level of the  $\tilde{B}(2)$  state shown in Figure 4a. These transitions will be discussed further in section 5.

Spectra recorded via the same rotational level, but differing vibrational levels of the  $\tilde{B}$  state can be compared in Figure 6. There are only rather subtle changes in relative intensity of the rotational transitions on changing the vibrational state, implying that any vibrational autoionization mechanisms in play must display essentially the same dependence on rotational level for

each vibrational quantum number. Such an observation is consistent with previous studies of the vibrationally autoionizing states,<sup>26–30</sup> none of which observed any rotational dependence of the vibrational autoionization efficiency. In principle, vibrational couplings could perturb the observed intensities in the different vibrational bands either through lifetime effects (high- $n$  Rydberg decay by vibrational autoionization) or by bound-state couplings between the high- $n$  Rydberg states and low- $n$  interlopers of different  $v_2^+$ .

### 3. Multichannel Quantum Defect Theory Simulation of the Spectra

**3.1. MQDT Formulation and Application to MATI/ZEKE Spectra.** To simulate a MATI or ZEKE spectrum we need to calculate the excitation probability to the long-lived Rydberg states that are subsequently field ionized. The quantity required is a *partial* cross-section in the sense that there are normally degenerate continua associated with lower lying ionization thresholds that can also be excited either directly or indirectly. These continua will give rise to prompt electrons/ions upon excitation, which are not detected in the ZEKE/MATI experiment. Although the pseudocontinua of high- $n$  Rydberg states are *closed* channels with respect to ionization, in practice it is easier to calculate the partial photoionization cross section into an open channel than the absorption cross section to the very high- $n$  Rydberg states. The procedure followed below is therefore to treat the pseudocontinuum below threshold as a true continuum. The threshold of interest is artificially lowered by the same amount as the lowering caused by the pulsed detection field. The partial photoionization cross section into a particular channel for energies between the lowered ionization threshold and the field-free threshold is then determined i.e., the partial photoionization cross section into the energy region sampled in the ZEKE or MATI experiment is calculated.

The procedure of artificially lowering the threshold of interest is justified on the grounds that (a) it is a fundamental tenet of MQDT that interactions between channels are approximately independent of energy and therefore continuous across threshold; (b) the transition intensity per unit energy should be a continuous function on passing through the threshold; and (c) the stabilization processes that allow the initially populated high- $n$  Rydberg states to evolve into the high- $m$  stabilized states can be considered as irreversible in the same sense that direct photoionization is irreversible. Any interactions between Rydberg states converging on different ion-core thresholds occur when the electron is initially in the core region where the high- $n$  Rydberg state is formed, and the ion-core quantum numbers are then unaltered in the delay period before field ionization, because the electron does not return to the core.

The method used here to calculate the partial photoionization cross sections is based on that described by Du and Greene,<sup>31</sup> who used it to analyze HD photoionization. The application of this method to simulate the ZEKE spectrum of H<sub>2</sub> was described by Softley and Hudson,<sup>13</sup> and the preliminary application to NH<sub>3</sub> is described in Paper I. In the following only the essential features and changes from the previous work are highlighted.

Following the approach of Du and Greene,<sup>31</sup> we set up an  $\mathcal{N} \times \mathcal{N}$  matrix of the quantum defect operator  $\boldsymbol{\mu}$  in the basis set of  $\mathcal{N}$ /Hund's case (d) long-range channels  $|i\rangle$ , including both open and closed channels. In the present work the label  $i$  represents the core quantum numbers  $N^+$ ,  $K^+$ ,  $v^+$ , the Rydberg electron quantum number,  $l$ , and the total angular momentum excluding spin,  $N$ . The off-diagonal matrix elements  $\mu_{ii'}$  encapsulate all the interactions between the channels.

The eigenvectors  $U_{i\alpha}$  and the eigenvalues  $\mu_\alpha$  obtained by diagonalization of the quantum defect matrix are employed in setting up a generalized eigenvalue equation

$$\boldsymbol{\Gamma}\mathbf{A} = \tan \pi\tau\boldsymbol{\Lambda}\mathbf{A} \quad (5)$$

with the matrix elements of  $\boldsymbol{\Gamma}$  and  $\boldsymbol{\Lambda}$  given by

$$\Gamma_{i\alpha} = U_{i\alpha}^{(N)} \sin \pi(v_i + \mu_\alpha^{(N)}), \quad \Lambda_{i\alpha} = 0, \quad \text{for } i \text{ closed} \quad (6)$$

$$\Gamma_{i\alpha} = U_{i\alpha}^{(N)} \sin \pi\mu_\alpha^{(N)}, \quad \Lambda_{i\alpha} = U_{i\alpha}^{(N)} \cos \pi\mu_\alpha^{(N)}, \quad \text{for } i \text{ open} \quad (7)$$

$\mathbf{A}$  is a matrix of coefficients in the expansion of the  $\mathcal{N}_O$  independent solutions of the Schrödinger equation ( $\mathcal{N}_O$  is the number of open channels) as linear combinations of the eigenchannel wave functions

$$\Psi_\rho = \sum_{\alpha=1}^{\mathcal{N}} A_{\alpha\rho}(E)\Psi_\alpha(E) \quad (8)$$

The coefficients  $A$  and the eigenphases  $\tau$  are used in the calculation of the partial photoionization cross section to produce the ion in state  $N^+$ ,  $K^+$ ,  $v^+$ .

$$\sigma_{N^+,K^+,v^+}(E) = \frac{4\pi^2\zeta\omega}{3(2J^+ + 1)} \sum_{Ni} |D_i^{(N)}(E)|^2 \quad (9)$$

where  $\omega$  is the photon energy in atomic units and  $\zeta$  the fine-structure constant.  $D_i^{(N)}(E)$  is the reduced dipole matrix element into a particular final channel  $|i\rangle$  with total angular momentum excluding spin  $\mathbf{N} = \mathbf{N}^+ + \mathbf{1}$ .

$$D_i^{(N)} = \sum_{\rho=1}^{\mathcal{N}_O} \exp(i\eta_i) T_{i\rho} \exp(i\pi\tau_\rho) D_\rho^{(N)} \quad (10)$$

The phase factor  $\eta_i$  disappears when taking the squared modulus in eq 9,

$$T_{i\rho}(E) = \sum_{\alpha=1}^{\mathcal{N}} U_{i\alpha}^{(N)} \cos \pi(-\tau_\rho + \mu_\alpha^{(N)}) A_{\alpha\rho} \quad (11)$$

and the  $D_\rho^{(N)}$  are expressed in terms of the  $D_\alpha^{(N)}$  by analogy with eq 8:

$$D_\rho^{(N)} = \sum_{\alpha=1}^{\mathcal{N}} D_\alpha^{(N)} A_{\alpha\rho} \quad (12)$$

The expression for the eigenchannel transition moments  $D_\alpha^{(N)}$  must be altered from that given in Paper I and is discussed below.

Equations 5–12 have an implicit energy dependence because of the appearance of  $v_i$ , the effective principal quantum number for the closed channels  $i$  in eq 6. The equations must therefore be evaluated on a fine energy grid over the ZEKE detection range for each threshold of interest.

**3.2. Construction of the Quantum Defect Matrix: Application of Molecular Symmetry Selection Rules.** As shown in eq 9, the partial photoionization cross section at a given threshold is calculated by summing the contributions from different possible values of Rydberg angular momentum  $l$  and the total angular momentum (excluding spin),  $N$ . A separate quantum defect matrix is constructed, and the calculation of the  $D_i^{(N)}$  repeated, for each value of  $N$  satisfying the selection

**TABLE 3: Rovibronic Symmetries for Given Total Vibronic Symmetry  $\Gamma_{ve}$** 

$\Gamma_{ve}$	$\Gamma_{Ryd}$	$K = 0$	1	2	3	4	5	6
$A_2''$	$sa_1', da_1'$	$A_2''$	$E'$	$E''$	$A_2'$	$E''$	$E'$	$A_2''$
$A_1'$	$pa_2''$	$A_1'$	$E''$	$E'$	$A_1''$	$E'$	$E''$	$A_1'$
$E''$	$pe', de'$	$E''$	$A_2' + E'$	$E'' + A_2''$	$E' + E'$	$A_2' + E''$	$E' + A_2'$	$E''$
$E'$	$de''$	$E'$	$A_2'' + E''$	$E' + A_2'$	$E'' + E''$	$A_2'' + E'$	$E'' + A_2''$	$E'$

<sup>a</sup> The vibronic symmetries in column 1 correspond to the Rydberg symmetries in column 2 when the latter are multiplied by the  $A_2''$  rovibronic symmetry of the ion-core ground state.

rule

$$N - J = 0, \pm 1 \quad (13)$$

The Hund's case (d) long-range channels which should be included are all those that obey the total rovibronic (rve) symmetry selection rules for the transition  $i \rightarrow f$ ,<sup>32</sup>

$$\Gamma_{rve}^i \otimes \Gamma_{rve}^f \supset \Gamma^* \quad (14)$$

The antisymmetric representation of the molecular symmetry group,  $\Gamma^*$ , transforms as  $A_1'$  in  $D_{3h}$ . Channel interactions will occur between levels of the same total symmetry, and therefore some channels must be included that might not obey the expected  $\Delta l = \pm 1$  selection rule from the intermediate state. The final state symmetry  $\Gamma_{rve}^f$  is resolved into a product of Rydberg electron and ion-core symmetries and, as pointed out by Signorell and Merkt,<sup>12</sup> in the long-range region, where the excited electron is completely decoupled from the ion core, the electronic wave function will be unaffected by the nuclear permutation operations. Hence the wave functions of even- $l$  Rydberg electrons will transform as the totally symmetric representation  $\Gamma^s$  of the molecular symmetry group while odd- $l$  Rydberg electron wave functions will transform as the antisymmetric representation  $\Gamma^*$ , i.e.,

$$\Gamma_{rve}^{ion} \otimes A_1'' \supset \Gamma_{rve}^f \quad \text{for } l \text{ odd}$$

$$\Gamma_{rve}^{ion} \otimes A_1' \supset \Gamma_{rve}^f \quad \text{for } l \text{ even}$$

We note in passing that this symmetry classification of the Rydberg electron wave function in the long-range region differs from that used by Müller-Dethlefs in reference 10. The following additional restrictions also apply to the channels that should be included:

- Nuclear spin symmetry is conserved throughout the transition i.e., *ortho*  $\leftrightarrow$  *ortho* and *para*  $\leftrightarrow$  *para* but *ortho*  $\nleftrightarrow$  *para*.
- The allowed values of  $N^+$  for given  $N$  and  $l$  are found by the relationship

$$N = N^+ + 1 \quad (15)$$

As an example, for the case of excitation via the  $\tilde{C}'(0) 2_1$  state, which has  $\Gamma_{rve}^i = E''$ , substituting into eq 14 gives

$$E'' \otimes \Gamma_{rve}^f \supset A_1''$$

implying

$$\Gamma_{rve}^f = E'$$

Thus, it is the channels with  $E'$  symmetry overall that must be included in the quantum defect matrix leading to

$$\Gamma_{rve}^{ion} = E'' \quad \text{for } l \text{ odd}$$

$$\Gamma_{rve}^{ion} = E' \quad \text{for } l \text{ even}$$

For even- $\nu_2$  vibronic states of the ion, the ion-core vibronic symmetry is  $\Gamma_{ve} \equiv A_2''$ , and is  $A_2'$ , for odd- $\nu_2$ . The rovibronic symmetries of the ion-core states  $\Gamma_{rve}^{ion}$  vary with the  $K^+$  quantum number, and these are listed for all possible vibronic symmetries in Table 3. By reference to row 1 it is evident that the channels accessible in the ground vibrational state (or states with even  $\nu_2$ ) of the ion are

$$K^+ = 2, 4 \quad \text{for } l \text{ odd } (E'' \text{ levels})$$

$$K^+ = 1, 5 \quad \text{for } l \text{ even } (E' \text{ levels})$$

all of which are para states as required. From eq 13, the total angular momentum in the state reached is  $N = 1-3$  for excitation from  $J = 2$ . Use of eq 15, together with the results above, leads to the final case (d) states  $|N^+K^+lN\rangle$  listed in Table 4 for excitation from the  $\tilde{C}'(0) 2_1$  level.

The multichannel quantum defect theory requires a frame transformation from these Hund's case (d) channels appropriate for the long-range region into the eigenchannel basis appropriate for the close-coupled core region, which is approximately Hund's case (b). The transformation must conserve the total rovibronic symmetry (i.e.,  $E'$  in the example given above). In contrast to its behavior in the long-range region, the Rydberg electron wave function is affected by the symmetry properties of the molecular framework when in the core region and it transforms according to the irreducible representations of the  $s, p, d$ , etc. orbitals in the  $D_{3h}$  group, as listed in Table 1 and ref 23. To determine which Hund's case (b) type channels are to be included, we proceed as follows. First, the possible total vibronic symmetries  $\Gamma_{ve}$  for each value of  $l$  included in the long-range quantum defect matrix are determined by taking the product of the Rydberg and ion-core vibronic symmetries:

$$\Gamma_{ve} = \Gamma_{ve}^{ion} \otimes \Gamma_{Ryd} \quad (16)$$

where for the ground-state ion,  $\Gamma_{ve}^{ion} = A_2''$ . For example the Rydberg electron symmetries  $sa_1', pa_2''$  and  $pe'$  give total vibronic symmetries  $\Gamma_{ve} \equiv A_2'', A_1'$  and  $E''$  respectively for the ionic ground state. For each of these total electronic symmetries, we then find all the rovibronic states with the appropriate total symmetry ( $E'$  in the above example) from the listings in Table 3. Table 5 lists the result for the  $E'$  states with  $N = 1$  to 3. It should be noted that the total number of states in both Tables 4 and 5 is 46 including degeneracies; this equality must occur for all symmetries because the frame-transformation is represented by a square matrix, and there must also be the same number in each table with a given total angular momentum  $N$ .

In Du and Greene's work<sup>31</sup> applicable to diatomic molecules, the eigenstates of the quantum defect matrix, have a definite projection  $\lambda$  of the Rydberg electronic angular momentum along the internuclear axis;<sup>31</sup> this was assumed to be a good approximation in the case of ammonia also in Paper I. However, in  $D_{3h}$  symmetry  $\lambda$  is not strictly a good quantum number and

**TABLE 4: Case (d) Channels of  $E'$  Symmetry Accessible via the  $\tilde{C}'(0) 2_1$  State (even- $\nu_2$  Channels Only)**

$N^+$	$K^+$	1	$N$
1	1	0	1
2	1	0	2
3	1	0	3
2	2	1	3,2,1
3	2	1	3,2
4	2	1	3
4	4	1	3
1	1	2	3,2,1
2	1	2	3,2,1
3	1	2	3,2,1
4	1	2	3,2
5	1	2	3
5	5	2	3

**TABLE 5: Case b Channels (even- $\nu_2$ ) Accessible via the  $\tilde{C}'(0) 2_1$  State with  $E'$  Symmetry<sup>a</sup>**

$l\lambda$	$\Gamma_{ve}$	$K$	$N$
$s\sigma(a'_1)$	$A''_2$	1	1,2,3
$p\sigma(a'_2)$	$A''_1$	2	2,3
$p\pi(e')$	$E''$	1	1,2,3
		3*	3
$d\sigma(a'_1)$	$A''_2$	1	1,2,3
$d\pi(e'')$	$E''$	0	1,2,3
		2	2,3
$d\delta(e')$	$E''$	1	1,2,3
		3*	3

<sup>a</sup> There is a double-degeneracy associated with each value of  $N$ , excepting those marked “\*” for which there is a quadruple degeneracy.

instead the eigenstates  $|\alpha\rangle$  i.e., the close-coupling basis should be classified according to the Rydberg electron symmetry in  $D_{3h}$ , represented by  $\Gamma^{\text{Ryd}}$ . For example the channels represented in  $D_{\infty h}$  by the Rydberg electron quantum numbers  $p\pi$  and  $d\delta$  both correlate with  $e'$  symmetry in  $D_{3h}$  (see above), and therefore the eigenchannels of this symmetry may have mixed  $p\pi$  and  $d\delta$  character. This effect shows itself in the character of the  $\tilde{B}$  state, from which the transitions arising originate from both the  $p\pi$  and  $d\delta$  components of the  $e'$  orbital.

To incorporate this  $l\lambda$  mixing effect into the behavior of the high- $n$  Rydberg states and continua, the elements of the quantum defect matrix are written (in a generalization of the formalism given in paper I),

$$\mu_{\nu^+ N^+ K^+ l, \nu'^+ N'^+ K'^+ l'}^{(N)} = \sum_{\Gamma} \sum_{l\lambda, l'\lambda'(\Gamma)} \langle N^+ K^+ | \lambda K \rangle^{(lN)} \times \int [dR \langle \nu^+ | R \rangle^{(N^+ K^+)} \mu_{l\lambda, l'\lambda'}^{\Gamma}(R) \langle R | \nu'^+ \rangle^{(N'^+ K'^+)}] \langle l' K' | N'^+ K'^+ \rangle^{(l'N')} \quad (17)$$

where the notation  $\sum_{\Gamma} \sum_{l\lambda, l'\lambda'(\Gamma)}$  represents a sum over the possible Rydberg electron symmetries  $\Gamma$  and, for each symmetry, a further sum over the allowed  $l\lambda$  combinations (see Table 1) (e.g.,  $p\pi$ ,  $d\delta$  for  $\Gamma \equiv e'$ ,  $s\sigma$ ,  $d\delta$  for  $\Gamma \equiv a'_1$ ).

In eq 17  $\langle \nu^+ | R \rangle^{(N^+ K^+)}$  represents the vibrational frame transformation and is given directly by the vibrational wave function of the ion core in the long-range state  $|i\rangle$ . The rotational part of the frame transformation,  $\langle N^+ K^+ | \lambda K \rangle^{(lN)}$ , is given by

$$\langle N^+ K^+ | \lambda K \rangle^{(lN)} = (-1)^{N^+ + \lambda - N^+} \left( \frac{2}{1 + \delta_{K0}} \right)^{1/2} (2N^+ + 1)^{1/2} \begin{pmatrix} l & N & N^+ \\ -\lambda & K & -K^+ \end{pmatrix} \quad (18)$$

**TABLE 6: Values of the Diagonal Quantum Defects Used in the Simulations**

$ l\lambda\rangle$	$s\sigma$	$p\sigma$	$p\pi$	$d\sigma$	$d\pi$	$d\delta$	$f\sigma, f\pi, f\delta, f\phi$
$\mu$	0.89 <sup>a</sup>	0.5 <sup>b</sup>	0.81 <sup>b</sup>	0.06 <sup>c</sup>	0.025 <sup>c</sup>	0.08 <sup>d</sup>	0.0

<sup>a</sup> Reference 27. <sup>b</sup> Reference 34. <sup>c</sup> Reference 35. <sup>d</sup> Determined by fitting to experimental data, as discussed in text.

As written above, the quantum defect matrix  $\mu_{\nu^+ N^+ K^+ l, \nu'^+ N'^+ K'^+ l'}^{(N)}$  allows for the possibility of coupling between states of differing vibrational quantum number,  $\nu^+$ . Inclusion of this vibrational interaction allows the effect of vibrational autoionization and the relative intensities in different vibrational bands accessed via the same intermediate state to be calculated. However, the spectra reported here were only recorded in the energy range corresponding to vibrationally diagonal transitions, and the MATI spectra show no evidence for vibrational coupling, even though  $\Delta\nu_2 = -1$  vibrational autoionization is known to occur.<sup>26–28</sup> This is illustrated by the remarkable similarity between the spectra recorded via the same rotational levels of the differing vibrational components of the  $\tilde{B}$  state shown in Figure 5. The term in square brackets in eq 17 was therefore approximated by a single  $R$ -independent quantum defect parameter  $\mu_{l\lambda, l'\lambda'}^{\Gamma}$ , and the matrix elements of  $\mu$  off-diagonal in vibrational quantum number are ignored.

The diagonal quantum defects  $\mu_{l\lambda, l\lambda}^{\Gamma}$  are approximated by the spectroscopic quantum defects for low- $l$  states of the appropriate symmetry obeying Hund's case (b). Spectroscopic studies by Glowonia et al.<sup>33</sup> of the  $n = 3$  and 4 Rydberg states and by Langford et al.<sup>34</sup> and Cramb and Wallace<sup>27</sup> on higher  $n$  states have provided values for the  $s$ ,  $p$ , and  $d$  quantum defects for different values of  $n$ . The  $s\sigma$  series show some variation in the value of  $\mu$  with principal quantum number  $n$ . Although most of the values are close to 0.89, occasional values are much smaller or larger. These anomalies are attributed to configuration mixing in the core region and the value of 0.89 is used in the studies presented here. Of the  $s$ ,  $p$ , and  $d$  quantum defects, only the  $d\delta$  is undetermined. The  $nd\delta$  Rydberg states are yet to be seen spectroscopically, presumably because they are optically inaccessible from the ground state, and so the  $d\delta$  quantum defect is used as a variable parameter in our calculations. Values of the quantum defects used in the simulations are listed in Table 6.

The off-diagonal matrix elements  $\mu_{l\lambda, l'\lambda'}^{\Gamma}$  are only included for the  $p\pi/d\delta$  interaction. A mixing angle  $\theta$  is introduced, following a similar treatment to that used by Fredin et al. to analyze spectra of the  $s$  and  $d$  Rydberg series in NO.<sup>36</sup>

$$\mu_{l\lambda, l'\lambda'}^{\Gamma} = \sum_{\alpha} \langle l\lambda | \alpha \rangle^{\Gamma} \mu_{\alpha}^{\Gamma} \langle \alpha | l'\lambda' \rangle^{\Gamma} \quad (19)$$

where the  $|\alpha\rangle$  are the true electronic eigenchannels, labeled according to their dominant angular momentum component “ $l\lambda$ ”. The elements  $\langle l\lambda | \alpha \rangle$  of the frame transformation are given by

$$\begin{aligned} \langle l\lambda | \alpha \rangle^{\Gamma} &= \delta_{l\lambda, \alpha} & \text{for } \Gamma \neq e' \\ \langle p\pi | p\pi' \rangle^{e'} &= \langle d\delta | d\delta' \rangle^{e'} = \cos \theta \\ -\langle p\pi | d\delta' \rangle^{e'} &= \langle d\delta | p\pi' \rangle^{e'} = \sin \theta \end{aligned} \quad (20)$$

Mixing between other  $|l\lambda\rangle$  channels of the same symmetry, e.g.,  $s\sigma/d\sigma$ ,  $d\pi/f\delta$ , is assumed to be negligible since no evidence for it is seen in the spectra.

**3.3. The Dipole Matrix Elements.** To incorporate the  $p\pi/d\delta$  mixing, the eigenchannel transition moments are written in

**TABLE 7: Radial Dipole Matrix Elements for Final Rydberg Electron Symmetries Accessible from the  $\tilde{B}$  State<sup>38</sup>**

$\tilde{B}$ state character ( $l'\lambda'$ )	final Rydberg electron symmetry	$d_0$ <sup>38</sup>
$p\pi$	$s\sigma$	0.06
$p\pi$	$d\sigma, d\pi, d\delta$	0.217
$d\delta$	$p\pi$	0.314
$d\delta$	$f\pi, f\delta, f\phi$	0.402

the form (again generalizing the previous expressions in Paper I):

$$D_{\alpha}^{(N)} = \sum_i (U^T)_{\alpha i}^{(N)} \sum_{\Gamma} \sum_{l\lambda(\Gamma)} \langle N^+ K^+ | K\lambda \rangle^{(N)} \sum_{\alpha} \langle l\lambda | \alpha \rangle^{\Gamma} \times \langle \alpha | \mathbf{r} | J' K' \lambda' \rangle \quad (21)$$

The transition moment  $\langle \alpha | \mathbf{r} | J' K' \lambda' \rangle$  to the eigenchannel  $|\alpha\rangle$  is approximated by the dipole transition moment between two Hund's case (b) states  $\langle NK\lambda | \mathbf{r} | J' K' \lambda' \rangle$  an expression for which is given in ref 37. Here an analogous equation is used to that given in ref 37, without explicit consideration of parity, in which each of the quantum numbers  $\lambda$ ,  $K^+$ ,  $K$ , and  $K'$  can be positive or negative:

$$\langle NK\lambda | \mathbf{r} | J' K' \lambda' \rangle = \left[ \frac{1}{3} (2N+1)(2J'+1)(2l+1)(2l'+1) \right]^{1/2} \times \sum_v \begin{pmatrix} l & 1 & l' \\ 0 & 0 & 0 \end{pmatrix} \begin{pmatrix} l & 1 & l' \\ \lambda & v & \lambda' \end{pmatrix} \begin{pmatrix} N & 1 & J' \\ K & v & -K' \end{pmatrix} d_0 \quad (22)$$

where  $v$  can take the values  $-1$ ,  $0$ , or  $1$  and  $d_0$  is a one-electron radial integral determined as described below.

For the excitation from the  $3p\sigma$  orbital of the  $\tilde{C}'$  state,  $s\sigma$ ,  $d\sigma$  and  $d\pi$  Rydberg Hund's case (b) channels are accessible according to eq 22. Hence if the  $d_0$  are viewed as  $\lambda$ -independent parameters, only the ratio of  $p \rightarrow d$  to  $p \rightarrow s$  radial integrals needs to be found. This ratio has been determined by Townsend and Reid from studies of photoelectron angular distributions when exciting via the  $\tilde{B}$  state of  $\text{NH}_3$ .<sup>38</sup> They quote a value for  $d_0(p \rightarrow d):d_0(p \rightarrow s)$  of 3.6:1. Use of this value in the simulations described in section 4 gives satisfactory agreement with experiment. In addition, the above ratio was obtained from excitation from the  $\tilde{B}$  state, which has  $p\pi$  character. The fact that this ratio satisfactorily reproduces the spectrum when exciting from the  $p\sigma$   $\tilde{C}'$  state supports the assumption that the radial integrals can be taken as independent of  $\lambda$ .

For excitation via the  $\tilde{B}$  state, the Rydberg electron symmetries accessible, and the relative magnitude of the radial integrals  $d_0$  determined from the work of Townsend and Reid,<sup>38</sup> are shown in Table 7. Again use of these ratios provides satisfactory agreement with experiment.

#### 4. Results of MQDT Simulations of Spectra via the $\tilde{C}'$ State

An MQDT simulation of the MATI spectrum via the  $\tilde{C}'(0)$   $1_0$  state, is presented in Figure 8b, using the quantum defects given in Table 6, but setting the off-diagonal mixing angle  $\theta$  to zero. The partial photoionization cross section into each channel is calculated over a ZEKE bandwidth of  $7 \text{ cm}^{-1}$  and each box function is convoluted with a Gaussian line width of  $1 \text{ cm}^{-1}$  to give an overall peak shape. The MATI peaks observed experimentally are not normally Gaussian in shape; in many cases they have a sharp rise to the blue side of the peak, a region of approximately constant intensity then a gradual falling off to the red side. Although the rapid rise to the blue edge of the

peak is well simulated by the Gaussian line width, no attempt has been made to simulate the characteristic MATI peak shape including the falling off to the red side. Intensities to the red side of peaks in the calculated spectra may therefore appear too large.

Examination of Figure 8a,b shows that both the relative peak intensities and the structure within the  $0_0$  peak are well reproduced by the simulation. To demonstrate the role of the quantum defect as a measure of the extent of mixing between the long-range channels within the core region, Figure 8c shows a simulation in which all the quantum defects have been set to zero. Here, as expected, the channel interactions disappear. There is no transition intensity into the "forbidden"  $4_0$  channel, and the substructure within the  $0_0$  peak no longer appears. Direct excitation to the  $2_0$  state is dominant, supporting the proposition that the substructure in the  $0_0$  peak is due to intensity borrowing from the stronger optical transition to the  $2_0$  state. It is evident that the quantum defects control the branching ratio into the differing Hund's case d channels.

The value of the  $d\delta$  quantum defect, the only one as yet unknown, is assumed to lie between  $-0.1$  and  $+0.1$ . Within this range, the simulations are not very sensitive to its exact value. By varying the value of  $\mu_{d\delta}$  manually and comparing the resulting simulations with the experimental results for the four MATI spectra via the  $\tilde{C}'$  state, a 'best-fit' value of  $\mu_{d\delta} = +0.08$  was obtained. This value was used throughout the remainder of the simulations.

Simulations of the other spectra obtained via the  $\tilde{C}'$  state are shown in Figure 9, in each case employing a value of  $+0.08$  for  $\mu_{d\delta}$ . Again the relative peak intensities and substructure within the main peaks show good agreement between theory and experiment. In particular, the substructure within the  $1_1$  peak of the spectrum via the  $\tilde{C}'(0)$   $1_1$  intermediate (Figure 9a), is well simulated by the MQDT approach. A characteristic of each of the spectra is the greater intensity in the transition to the lowest  $N^+$  level. The MQDT simulations make it clear that this effect is due to "intensity borrowing" from Rydberg series converging on higher rotational thresholds. For example, it is possible to identify the origin of the very narrow, intense feature within the  $1_0$  peak of the spectrum via the  $\tilde{C}'(1)$   $2_0$  state shown in Figure 9c. By following the Rydberg series observed in the partial photoionization cross section into the  $1_0$  channel at energies as far as  $100 \text{ cm}^{-1}$  above threshold, it is apparent that the "spike" arises due to intensity borrowing from a Rydberg state belonging to the series converging on the  $3_0$  threshold.

**4.1.  $p\pi/d\delta$  Mixing.** In both Figures 8 and 9 the mixing angle, representing the  $p\pi/d\delta$  interaction is set to zero. Inspection of these figures shows that in each case, one or more small peaks are not reproduced in the simulations. These are the peaks produced from transitions with values of  $\Delta K^+$  forbidden according to the zero-order selection rules discussed in section 2.2.1. For example, in the spectra produced via the intermediate states with  $K' = 0$  (Figures 8 and 9c),  $K^+ = 3$  peaks are seen, while in those via  $K' = 1$  (Figure 9a and b),  $K^+ = 2$  peaks are evident, neither of which are reproduced in the simulations as presented so far. By inspection of Table 4, in which the case d channels accessible via the  $\tilde{C}'(0)$   $2_1$  state are listed, it can be seen that the "forbidden" peaks are those associated with an  $l$  quantum number of 1, i.e., a  $p$  Rydberg electron. Given that the selection rule on the electronic part of the transition is  $\Delta l = \pm 1$ , there can be no direct transition intensity to these states from the  $3p\sigma$  intermediate. Instead they must be appearing as a result of the  $p\pi/d\delta$  final-state mixing. Figure 10 shows the effect of increasing the mixing angle  $\theta$  in eq 20 from zero in the spectrum via the  $\tilde{C}'(0)$   $1_1$  state. As expected, increasing  $\theta$  allows

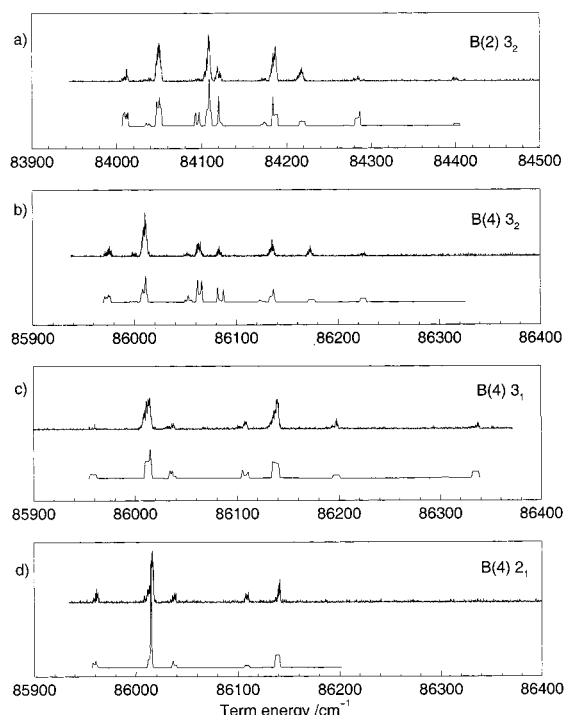


**Figure 12.** MATI spectra (upper trace) and MQDT simulations (lower trace), including a  $p\pi/d\delta$  mixing angle of  $5^\circ$ , via a) the  $\tilde{B}(2) 3_2$  level, (b) the  $\tilde{B}(4) 3_2$  level, (c) the  $\tilde{B}(4) 3_1$  level and (d) the  $\tilde{B}(4) 2_1$  level. (Assignment given in Figures 4–6).

transfer of intensity between the transitions to the  $d$  and the  $p$  states and hence increases the magnitude of the  $K^+ = 2$  peaks. An optimum mixing angle of  $5^\circ$  was found to give the best agreement between simulation and experiment, and Figures 11a to c show the improvements obtained in introducing the mixing angle in the simulations of the other spectra via the  $\tilde{C}'$  state. All peaks seen experimentally are now simulated with the correct intensities, illustrating the power of the MQDT method.

### 5. Results of MQDT Simulations of Spectra via the $\tilde{B}'$ State

Simulations of the spectra recorded via the  $\tilde{B}$  state were also carried out, using the same parameters as the simulations via the  $\tilde{C}'$  state i.e., a  $d\delta$  quantum defect of +0.08 and a  $p\pi/d\delta$  mixing angle,  $\theta$ , of  $5^\circ$ , and are shown in Figure 12. The dominant transitions in each spectrum are those originating from the  $p\pi$  component of the  $\tilde{B}$  state i.e., the  $\Delta K^+ = \pm 1$  transitions, with less intense  $\Delta K^+ = \pm 2$  transitions originating from the  $d\delta$  component of the  $\tilde{B}$  state. As well as reproducing the 'allowed' transitions, the MQDT simulations also show intensity into the 'forbidden' peaks associated with large changes in rotational quantum number,  $\Delta N^+$ . The introduction of the final-state  $p\pi/d\delta$  mixing reveals the origin of the  $\Delta K^+ = 0$  transitions to  $K^+ = 2$  rotational states observed in the spectra recorded via the  $3_2$  state (Figure 4a and Figure 12a,b). These can be attributed, as in the MATI spectra via the  $\tilde{C}'$  state, to coupling between a channel  $|i\rangle$  associated with a  $d$  photoelectron and a channel  $|i'\rangle$  associated with a  $p$  photoelectron, i.e., the  $3_2$  and  $2_2$  peaks in the spectrum via the  $\tilde{B}(2) 3_2$  state, which according to the symmetry arguments of section 3.2 are associated with  $p$  photoelectrons, can gain intensity by coupling to the  $2_1$  and  $3_1$  states associated with a  $d$  photoelectron.

Since spectra recorded via the same rotational level but differing vibrational levels were so similar in each case, only the spectrum via one vibrational level is compared to the

simulation in Figure 12 for the excitation from the  $3_1$  and  $2_1$  levels. Similar agreement was obtained in simulations of the other vibrational levels. In Figure 12a,b, a comparison is made for the excitation via the  $\tilde{B}(2)$  and  $\tilde{B}(4) 3_2$  levels, and it is shown that the subtle differences in the experimental spectra are quite well accounted for by rotational coupling only. Overall, it was found that the best reproduction of the experimental spectra was obtained with the dipole matrix elements for excitation out of the  $d\delta$  component of the  $\tilde{B}$  state weighted by a factor of 0.5 compared to those for excitation out of the  $p\pi$  component, i.e., assuming a two-thirds  $p\pi$ , one-third  $d\delta$  character for the intermediate state. Again the MQDT theory provides a good reproduction of the experimental data.

### 6. Conclusions

This paper has presented a modeling of the MATI spectra of ammonia using Multichannel Quantum Defect Theory. The theoretical simulations show very encouraging agreement with the experimental data, even though vibrational couplings are ignored, suggesting that this method provides a good approach to accurate modeling of intensities in ZEKE or MATI spectra. The calculations also enable us to estimate values for the  $d\delta$  quantum defect ( $\mu_{d\delta} = +0.08$ ) and the  $p\pi/d\delta$  mixing angle in the high  $n$  Rydberg states ( $\theta = 5^\circ$ ). The mixing angle represents the extent to which the  $l$  quantum number remains good when the Rydberg electron is sufficiently close to interact with the core electrons, a form of configuration interaction.

One factor omitted from the MQDT calculations is the presence of the discrimination field, which could lead to additional couplings. However, Merkt et al. have demonstrated that electric field induced couplings are unlikely to play a significant role in molecules with large rotational constants.<sup>39</sup> The success of the simulations without inclusion of any electric field effects adds weight to this hypothesis.

Multichannel quantum defect theory is the only method currently available which is able to model rotational line intensities when bound-state channel couplings play a role. The fact that this is achieved in the present case using a handful of quantum defect parameters suggests that ZEKE and MATI spectroscopies should be regarded as fully interpretable techniques.

### References and Notes

- (1) Dickinson, H.; Rolland, D.; Softley, T. P. *Philos. Trans. R. Soc. London A* **1997**, *355*, 1585.
- (2) Müller-Dethlefs, K.; Sander, M.; Schlag, E. W. *Chem. Phys. Lett.* **1984**, *112*, 291.
- (3) Schlag, E. W. *ZEKE Spectroscopy*; Cambridge University Press: Cambridge, 1998.
- (4) Zhu, L.; Johnson, P. M. *J. Chem. Phys.* **1991**, *94*, 5769.
- (5) Signorell, R.; Merkt, F. *Faraday Discuss* **2000**, *115*, 205.
- (6) Lee, M.-T.; Wang, K.; McKoy, V.; Tonkyn, R. G.; Wiedmann, R. T.; Grant, E. R.; White, M. G. *J. Chem. Phys.* **1992**, *96*, 7848.
- (7) Lee, M.-T.; Wang, K.; McKoy, V. *J. Chem. Phys.* **1992**, *97*, 3108.
- (8) Lee, M.-T.; Wang, K.; McKoy, V.; Machado, L. E. *J. Chem. Phys.* **1992**, *97*, 3905.
- (9) Wang, K.; Lee, M.-T.; McKoy, V.; Wiedmann, R. T.; White, M. G. *Chem. Phys. Lett.* **1994**, *219*, 397.
- (10) Müller-Dethlefs, K. *J. Chem. Phys.* **1991**, *95*, 4821.
- (11) Habenicht, W.; Reiser, G.; Müller-Dethlefs, K. *J. Chem. Phys.* **1991**, *95*, 4809.
- (12) Signorell, R.; Merkt, F. *Mol. Phys.* **1997**, *92*, 793.
- (13) Softley, T. P.; Hudson, A. J. *J. Chem. Phys.* **1994**, *101*, 923.
- (14) Conaway, W. E.; Morrison, R. J. S.; Zare, R. N. *Chem. Phys. Lett.* **1985**, *113*, 429.
- (15) Morrison, R. J. S.; Conaway, W. E.; Zare, R. N. *Chem. Phys. Lett.* **1985**, *113*, 435.
- (16) Nieman, G. C.; Colson, S. D. *J. Chem. Phys.* **1979**, *71*, 571.
- (17) Ashfold, M. N. R.; Dixon, R. N.; Stickland, R. J. *Chem. Phys.* **1984**, *88*, 463.

- (18) Ashfold, M. N. R.; Dixon, R. N.; Little, N.; Stickland, R. J.; Western, C. M. *J. Chem. Phys.* **1988**, *89*, 1754.
- (19) Softley, T. P.; Rednall, R. J. *J. Chem. Phys.* **2000**, *112*, 7992.
- (20) Niu, B. H.; White, M. G. *J. Chem. Phys.* **1996**, *104*, 2136.
- (21) Reiser, G.; Habenicht, W.; Müller-Dethlefs, K. *J. Chem. Phys.* **1993**, *98*, 8462.
- (22) Lee, D. S.; Oka, T. *J. Chem. Phys.* **1991**, *94*, 1698.
- (23) Herzberg, G. *Molecular Spectra and Molecular Structure Volume II. Infrared and Raman Spectra of Polyatomic Molecules*; Krieger: Malabar, FL, 1991.
- (24) Merkt, F.; Softley, T. P. *Int. Rev. Phys. Chem.* **1993**, *12*, 205.
- (25) Douglas, A. E. *Discuss. Faraday Soc.* **1963**, *35*, 158.
- (26) Glowonia, J. H.; Riley, S. J.; Colson, S. D.; Miller, J. C.; Compton, R. N. *J. Chem. Phys.* **1982**, *77*, 68.
- (27) Cramb, D. T.; Wallace, S. C. *J. Chem. Phys.* **1994**, *101*, 6523.
- (28) Raptis, C. A.; Pratt, S. T. *Chem. Phys. Lett.* **1999**, *303*, 281.
- (29) Raptis, C. A.; Bacon, J. A.; Pratt, S. T. *J. Chem. Phys.* **2000**, *112*, 2815.
- (30) Bacon, J. A.; Pratt, S. T. *J. Chem. Phys.* **2000**, *112*, 4153.
- (31) Du, N. Y.; Greene, C. H. *J. Chem. Phys.* **1986**, *85*, 5430.
- (32) Bunker, P. R. *Molecular Symmetry and Spectroscopy*; Academic Press: New York, 1979.
- (33) Glowonia, J. H.; Riley, S. J.; Colson, S. D.; Nieman, G. C. *J. Chem. Phys.* **1980**, *73*, 4296.
- (34) Langford, S. R.; Orr-Ewing, A. J.; Morgan, R. A.; Western, C. M.; Ashfold, M. N. R.; Rijkenberg, A.; Scheper, C. R.; Buma, W. J.; de Lange, C. A. *J. Chem. Phys.* **1998**, *108*, 6667.
- (35) Li, X.; Vidal, C. R. *J. Chem. Phys.* **1995**, *102*, 9167.
- (36) Fredin, S.; Gauyacq, D.; Horani, M.; Jungen, Ch.; Lefevre, G.; Masnou-Seeuws, F. *Mol. Phys.* **1987**, *60*, 825.
- (37) Child, M. S.; Jungen, Ch. *J. Chem. Phys.* **1990**, *93*, 7756.
- (38) Townsend, D.; Reid, K. L. *J. Chem. Phys.* **2000**, *112*, 9783.
- (39) Merkt, F.; Fielding, H. H.; Softley, T. P. *Chem. Phys. Lett.* **1993**, *202*, 153.